Biointerface Research in Applied Chemistry
Open-Access Journal (ISSN: 2069-5837)

Article
Volume 16, Issue 1, 2026, 13
https://doi.org/10.33263/BRIAC161.013

Strategic Design and Synthesis of a Piperazine-Coupled 1,3-diketone as a Potential Antibacterial Agent Against MRSA

Ningaraju Gejjiganahalli Ningappa [1], Shanthappa Nanjundaswamy [1], Santhosh Arehalli Shivamurthy [2], Chimatahalli Shanthakumar Karthik [1,*]

[1] Department of Chemistry, SJCE, JSS Science and Technology University, Mysuru-570 006, Karnataka, India
[2] Department of Chemistry (U.G.), N.M.K.R.V. College for Women, Karnataka 560011, India
* Correspondence: csk@jssstuniv.in;

Received: 18.09.2025; Accepted: 1.11.2025; Published: 15.02.2026

Abstract: Methicillin-resistant *Staphylococcus aureus* (MRSA) poses a significant healthcare challenge due to its strong antibiotic resistance. In this study, a piperazine-coupled 1,3-diketone derivative, compound-1d ((2E,2′E)-2,2′-(piperazine-1,4-diylbis(methaneylylidene))bis(1-phenylbutane-1,3-dione)), was strategically designed, synthesized, and characterized using FT-IR, ^{1}H-NMR, and ^{13}C-NMR techniques. The compound exhibited significant antibacterial activity, with minimum inhibitory concentration (MIC) and minimum bactericidal concentration (MBC) of 125 µg/mL and 250 µg/mL, respectively, against MRSA (ATCC 43300). Computational analyses, including ADMET prediction, DFT calculations, molecular docking, and molecular dynamics simulations, confirmed strong and stable interactions with PBP2a (1MWT) and glycosyltransferase (6FTB) proteins, showing binding energies of -8.8 and -7.1 kcal/mol, respectively. The results demonstrate that the piperazine bridge plays a pivotal role in enhancing antibacterial activity, highlighting compound-1d as a promising lead scaffold that disrupts PBP2a- and glycosyltransferase-mediated cell wall synthesis in MRSA.

Keywords: piperazine; MRSA; bacterial resistance; molecular docking; molecular dynamics simulation.

© 2026 by the authors. This article is an open-access article distributed under the terms and conditions of the Creative Commons Attribution (CC BY) license (https://creativecommons.org/licenses/by/4.0/), which permits unrestricted use, distribution, and reproduction in any medium, provided the original work is properly cited. The authors retain copyright of their work, and no permission is required from the authors or the publisher to reuse or distribute this article, as long as proper attribution is given to the original source.

1. Introduction

Methicillin-resistant *Staphylococcus aureus* (MRSA) remains a primary global health concern due to its rapid evolution of antibiotic resistance and limited treatment options. Initially confined to hospital-acquired infections (HA-MRSA), MRSA has now spread into community environments (CA-MRSA), causing severe skin, respiratory, and soft-tissue infections associated with high morbidity and mortality [1,2]. The pathogen's resistance is primarily due to the mecA gene, which encodes penicillin-binding protein 2a (PBP2a), an enzyme that enables cell wall synthesis even in the presence of β-lactam antibiotics. In addition, virulence factors such as α-hemolysin, Panton–Valentine leukocidin (PVL), and phenol-soluble modulins (PSMα) contribute to its aggressiveness and immune evasion [3].

With conventional antibiotics such as Vancomycin, daptomycin, and linezolid increasingly failing, research has shifted toward small-molecule inhibitors that target essential

bacterial enzymes and membrane components [4]. Notably, compounds like WYBQ-4 and MZ-01 have demonstrated robust anti-MRSA activity by binding to PBPs and disrupting cell membrane integrity, while maintaining low cytotoxicity [2,3]. However, the emergence of cross-resistance and poor drug permeability underscores the need for new scaffolds with optimized physicochemical properties and enhanced target affinity.

Among these, piperazine-based frameworks have attracted attention for their structural flexibility, water solubility, and pharmacophoric adaptability [5]. Incorporating electron-withdrawing groups and heteroatoms improves lipophilicity and antibacterial potency. For instance, piperazine–phthalimide derivatives exhibited potent anti-MRSA activity (MIC = 45 ± 0.15 µg/mL), demonstrating membrane disruption validated by SEM and molecular docking [6]. Similarly, Schiff-base piperazine analogs achieved an MIC of 30 ± 0.45 µg/mL, with low cytotoxicity and favorable ADMET profiles [7].

Complementing this, the 1,3-diketone motif provides electron-delocalized carbonyl groups that facilitate hydrogen bonding and metal coordination at enzyme active sites, thereby ensuring strong ligand–receptor interactions [8]. Combining both moieties into a single scaffold provides a rational route for enhanced biological performance. Furthermore, diversity-oriented synthesis (DOS) approaches have yielded structurally diverse molecules with promising anti-MRSA profiles [9]. Unlike many previously reported piperazine-based analogs that employ aromatic, phthalimide, or imide linkers, compound-1d uniquely integrates a β-diketone moiety to enhance electron delocalization, conjugation, and hydrogen-bonding capability, thereby improving its binding interactions and physicochemical balance [5,10]. This hybrid scaffold was rationally designed to target two essential MRSA enzymes, PBP2a and glycosyltransferase, offering a dual mechanism of action through both cell-wall disruption and enzyme inhibition [11,12]. The incorporation of the β-diketone fragment provides electronic stabilization and facilitates stronger hydrogen bonding within active-site residues, an advantage not observed in conventional piperazine scaffolds [13]. To our knowledge, this represents one of the first piperazine-1,3-diketone hybrids validated through integrated *in silico* and *in vitro* analyses against MRSA, marking a significant design advancement in next-generation antibacterial scaffolds [14].

Building on these insights, the present study reports the design, synthesis, and characterization of a novel piperazine–1,3-diketone hybrid (compound 1d) and evaluates its antibacterial activity against MRSA. The compound was analyzed through *in silico* ADMET, DFT, molecular docking, and molecular dynamics simulations targeting PBP2a and glycosyltransferase, followed by *in vitro* MIC and MBC assays. This integrated approach establishes the piperazine–diketone scaffold as a mechanistically defined, dual-acting antibacterial agent, capable of combining membrane disruption with target-specific enzyme inhibition, a potential strategy to address antibiotic resistance in MRSA.

2. Materials and Methods

All chemicals used in the synthesis, including starting materials, were purchased from Sigma-Aldrich and used without further purification. Elemental analysis was performed using a Perkin-Elmer 2400 analyzer. UV–visible spectra were recorded on a UV-1900 Shimadzu spectrophotometer using a 1 cm quartz cell. FT-IR spectra were collected as KBr pellets on an Agilent Genzel 690 FT-IR spectrophotometer (4000-400 cm^{-1}). The ^{1}H NMR spectra were recorded on an Agilent 400 MHz NMR spectrometer using DMSO as the solvent and DMSO-d6 as the internal standard.

2.1. Library of designed ligands.

In this study, we designed four piperazine-based compounds targeting MRSA proteins to identify potent antibacterial agents (Figure 1). Molecular docking was conducted to assess the potential binding affinity of these compounds to MRSA proteins. The compound with the highest binding score was selected for synthesis, characterization, and detailed *in silico* and *in vitro* evaluation. A schematic diagram (Figure 2) summarizing the key steps from compound design, synthesis, and characterization to in silico and in vitro evaluation has been added.

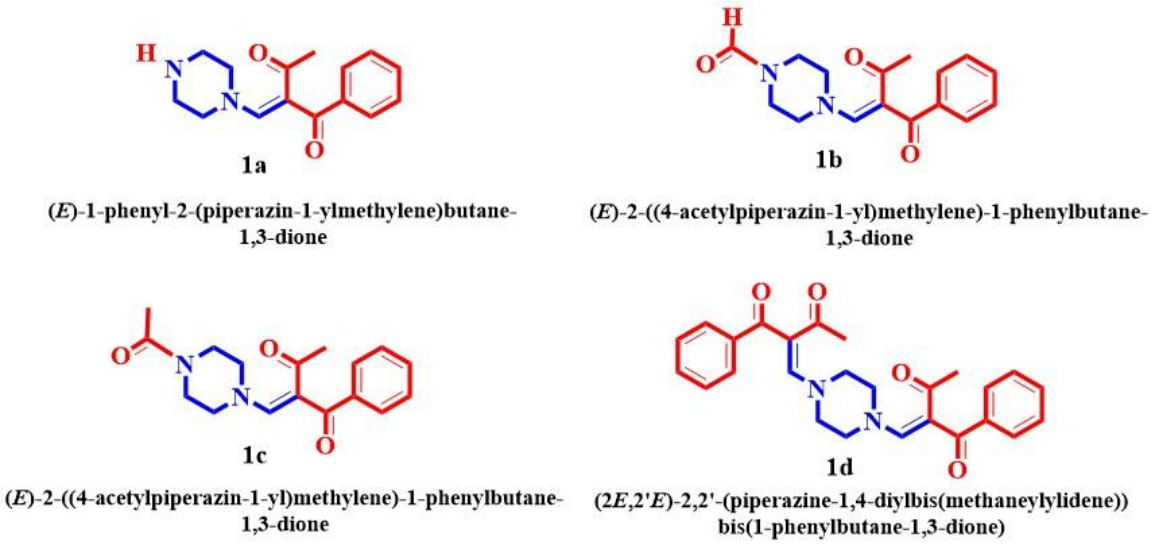

Figure 1. Designed piperazine-based compounds.

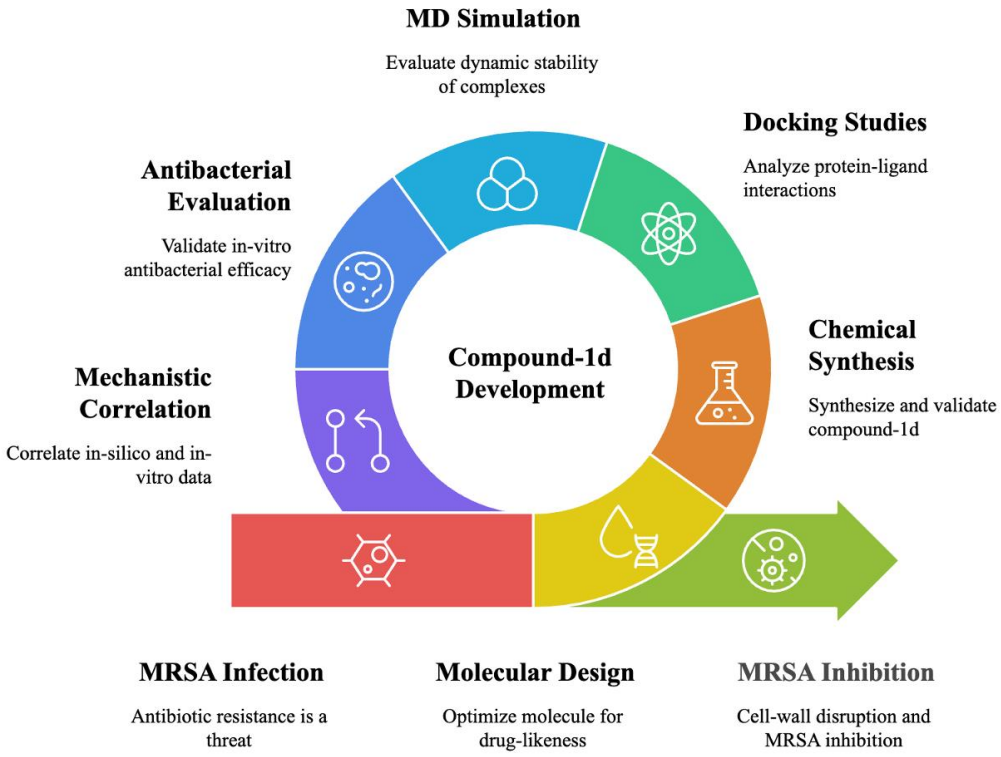

Figure 2. Schematic representation of the integrated experimental–computational workflow.

2.2. Synthesis of piperazine-coupled 1,3-diketone (compound-1d).

1-Phenylbutane-1,3-dione (0.1 g) was dissolved in methanol (5 mL), and triethylamine (0.5 mL) was added and refluxed for 15 min at ambient temperature. Then, piperazine-1,4-

dicarboxaldehyde (0.05 g) dissolved in 10 mL of methanol was added, and the reaction was refluxed for 24 hours. After 24 hours, 5-8 drops of pyridine were added, and the reflux continued for an additional 6 hours. TLC monitored the reaction. The solvent was evaporated under vacuum to obtain a white solid, which was recrystallized using methanol (Scheme 1). The reaction yield was 82%, with a melting point of 176-178°C, and purity was confirmed by TLC and NMR integration analysis.

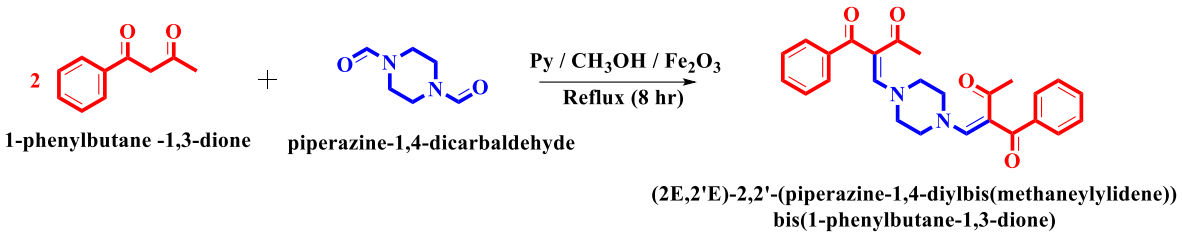

Scheme 1. Synthetic route.

2.3. ADMET prediction.

To evaluate the drug-likeness properties of the compound (2E,2′E)-2,2′-(piperazine-1,4-diylbis(methaneylylidene))bis(1-phenylbutane-1,3-dione), the SwissADME web tool was employed. This included assessment of its pharmacological profile and compliance with Lipinski's Rule of 5 and Veber's Rule [15]. The pkCSM online tool was also used to predict ADMET parameters, including intestinal absorption, skin permeability, blood–brain barrier permeability, CNS permeability, renal OCT2 interaction, Ames toxicity, and oral rat toxicity [16].

2.4. Density functional theory (DFT) studies.

The molecular structure of compound-1d was optimized using Gaussian 09 at the DFT/CAM-B3LYP++G(2d-p) level. Frontier molecular orbitals (HOMO-LUMO), energy gap, and global reactivity descriptors (electronegativity, hardness, softness, and electrophilicity) were determined using Koopman's approximation. The molecular electrostatic potential (MEP) surface was generated and visualized in GaussView 6.0.16 [17,18].

2.5. In-silico studies.

2.5.1. Molecular docking.

Molecular docking studies were conducted using the AutoDock Vina 1.5.6 tool. Ligand structures were initially created with ChemDraw and subsequently converted into the PDB format through Marvin JS software. Following this, all compounds were optimized and transformed into the PDBQT format using the AutoDock software [19]. The 3D structures of the target proteins, penicillin-binding protein (PBP2a) and Glycosyltransferase (GT), were obtained from the RCSB Protein Data Bank (PDB IDs: 1MWT and 6FTB), with the bound ligand removed using Biovia Discovery Studio 2019. Protein energies were minimized, and polar hydrogen atoms were added using the AutoDock method [20]. To identify binding sites, grid boxes were constructed for Glycosyltransferase (X = -46.10, Y = -32.10, Z = 62.88) and the PBP2a allosteric site (X = 13.33, Y = 30.36, Z = 23.67). The 3D structure of the compound was saved in PDB format with Marvin JS. Binding affinities were recorded as negative values in kilocalories per mole (kcal/mol), and protein-ligand interactions were analyzed and visualized using Biovia Discovery Studio 2019 [21]. Ligands with the highest binding scores

were isolated and listed for further analysis. Docking validation was ensured by maintaining an RMSD of ≤ 2.0 Å and verifying the grid box dimensions to confirm correct active-site coverage. Consensus scoring and redocking validation confirmed the reliability of the docking protocol.

2.5.2. Molecular dynamics simulation.

MD simulations were performed to evaluate the stability of the interaction between compound-1d and 1MWT and 6FTB proteins. GROMACS 2019.4, employing the GROMOS96 force field, was utilized for simulations on a GPU-enabled workstation [22]. Missing residues in the 1MWT and 6FTB structures were added using Discovery Studio. The system was set in a cubic box of 1.0 nm in size, solvated with water (SPC), and neutralized by the addition of sodium ions. Ligand topology files were generated using the PRODRG2 server, set up for the docked complex MD [23]. The system underwent energy minimization, followed by NVT and NPT equilibration (each for 100 ps) at 300 K and 1 bar, ensuring proper thermal and pressure stabilization. System stability was confirmed through RMSD plateau, total energy convergence, and steady-state temperature and pressure profiles. The system underwent energy minimization, temperature balancing (300 K), and pressure balancing (1 bar) for 100ns each, followed by 100ns of MD production runs, maintaining temperature at 300 K and pressure at 1 bar. Graphical representation and analysis of MD simulation data, including RMSD, RMSF, Rg, intermolecular hydrogen bonds, SASA, and Intra-molecular H-bonding, were performed using OriginPro 9.0 software.

2.6. Antibacterial studies.

The MRSA (ATCC 43300) bacterial strain was used to determine MIC and MBC.

2.6.1. Determination of minimum inhibitory concentration (MIC).

The antibacterial activity against the MRSA strain was evaluated using a modified broth microdilution procedure adapted from Agyare et al. [24]. In this assay, each well of a sterile 48-well microtiter plate was loaded with 200 µL of double-strength nutrient broth, after which the test samples were introduced at graded concentrations (250, 125, 62.5, 31.25, 15.625, and 7.8125 µg). Subsequently, 40 µL of the bacterial suspension (1×10^6 CFU/mL) was dispensed into each well, and the plates were incubated at 37 °C for 24 h. At the end of the incubation period, 40 µL of MTT reagent (3-(4,5-dimethylthiazol-2-yl)-2,5-diphenyltetrazolium bromide, 1.25 mg/mL) was added to every well. The plates were then incubated again under the same temperature conditions. A purple color signified metabolic activity, whereas pale or yellow wells signified the absence of viable bacterial cells after approximately 30 min. The MIC value was defined as the lowest concentration of the compound that produced no visible color change following the addition of MTT. All experiments were conducted in triplicate (n = 3), and results are presented as mean ± standard deviation (SD). The absorbance (OD_{570}) of each well was measured using a microplate reader to obtain quantitative data. Variation among replicates remained within 5%, confirming reproducibility and experimental reliability. The visual results were further confirmed by measuring the absorbance of each well at 570 nm and comparing it with that of the negative control well (organism without any treatment) as well as with the blank well (media and MTT solution alone).

2.6.2. Determination of minimum bactericidal concentrations (MBC).

The bactericidal effect was evaluated according to the procedure reported by Cos et al., with minor modifications [25]. In this method, each well of a 48-well microtiter plate was loaded with 200 µL of double-strength nutrient broth. The test compounds were then added at the specified concentrations (250, 125, 62.5, 31.25, 15.625, and 7.8125 µg), after which 40 µL of the bacterial inoculum (1×10^6 CFU/mL) was introduced into every well. The plates were incubated at 37 °C for 24 h. After 24 hours of incubation, aliquots (20 µL) were taken from each well and inoculated into freshly prepared 200 µL of nutrient broth, which was then incubated at 37°C for an additional 24 hours. After this step, 20 µL of MTT solution (3-(4,5-dimethylthiazol-2-yl)-2,5-diphenyltetrazolium bromide, 1.25 mg/mL) was added to the tubes. A purple color indicated bacterial viability, whereas clear or yellow solutions indicated complete growth inhibition. The MBC value corresponded to the lowest concentration of the compound that did not produce a color change, indicating the absence of detectable bacterial growth. The MBC was recorded as the lowest concentration, showing no visible bacterial growth. All assays were performed in triplicate (n = 3), and data were expressed as mean ± SD. The low standard deviation values (< 5%) confirmed the accuracy and reproducibility of MIC/MBC measurements.

3. Results and Discussions

3.1. Chemistry.

Synthesis of compound-1d was carried out by employing 1-phenylbutane-1,3-dione and piperazine-1,4-dicarbaldehyde as reactants. The identity of the synthesized compound-1d was ascertained through a comprehensive array of spectral analyses, including FT-IR, ^{1}H-NMR, and ^{13}C-NMR spectroscopy. The FT-IR spectrum (Figure 3a) revealed prominent absorption bands at 1610 cm^{-1} corresponding to the C=O stretching of the diketone moiety, 2900-3000 cm^{-1} assigned to C–H stretching vibrations of tertiary amine groups, and 1300-1400 cm^{-1} indicating aromatic C=C stretching in the phenyl ring. A strong band between 1200-1300 cm^{-1} also confirmed C–N stretching of the piperazine linkage, supporting successful coupling between the diketone and piperazine units. The ^{1}H-NMR spectrum (Figure 3b) recorded at 400 MHz in DMSO-d_6 showed distinct signals at δ 7.54-7.64 ppm (multiplets, aromatic protons), δ 3.43 ppm (t, CH_2 of the piperazine ring), and δ 2.33 ppm (s, CH_3 group attached to the carbonyl carbon). The presence of both aromatic and aliphatic proton resonances corroborated the proposed structure. The ^{13}C-NMR spectrum (Figure 3c) displayed characteristic signals at δ 163.5 ppm (C=O of the β-diketone), δ 135.0-129.0 ppm (aromatic carbons), and δ 47.7 ppm (methylene carbons of the piperazine ring), confirming the existence of both aromatic and heterocyclic fragments within the molecule. Additional peaks at δ 29.0 ppm corresponded to the methyl carbon adjacent to the carbonyl group, consistent with the expected molecular framework. Collectively, these spectral data unequivocally confirmed the successful synthesis of compound-1d, validating the presence of the piperazine-linked 1,3-diketone skeleton and demonstrating the reproducibility of the synthetic approach.

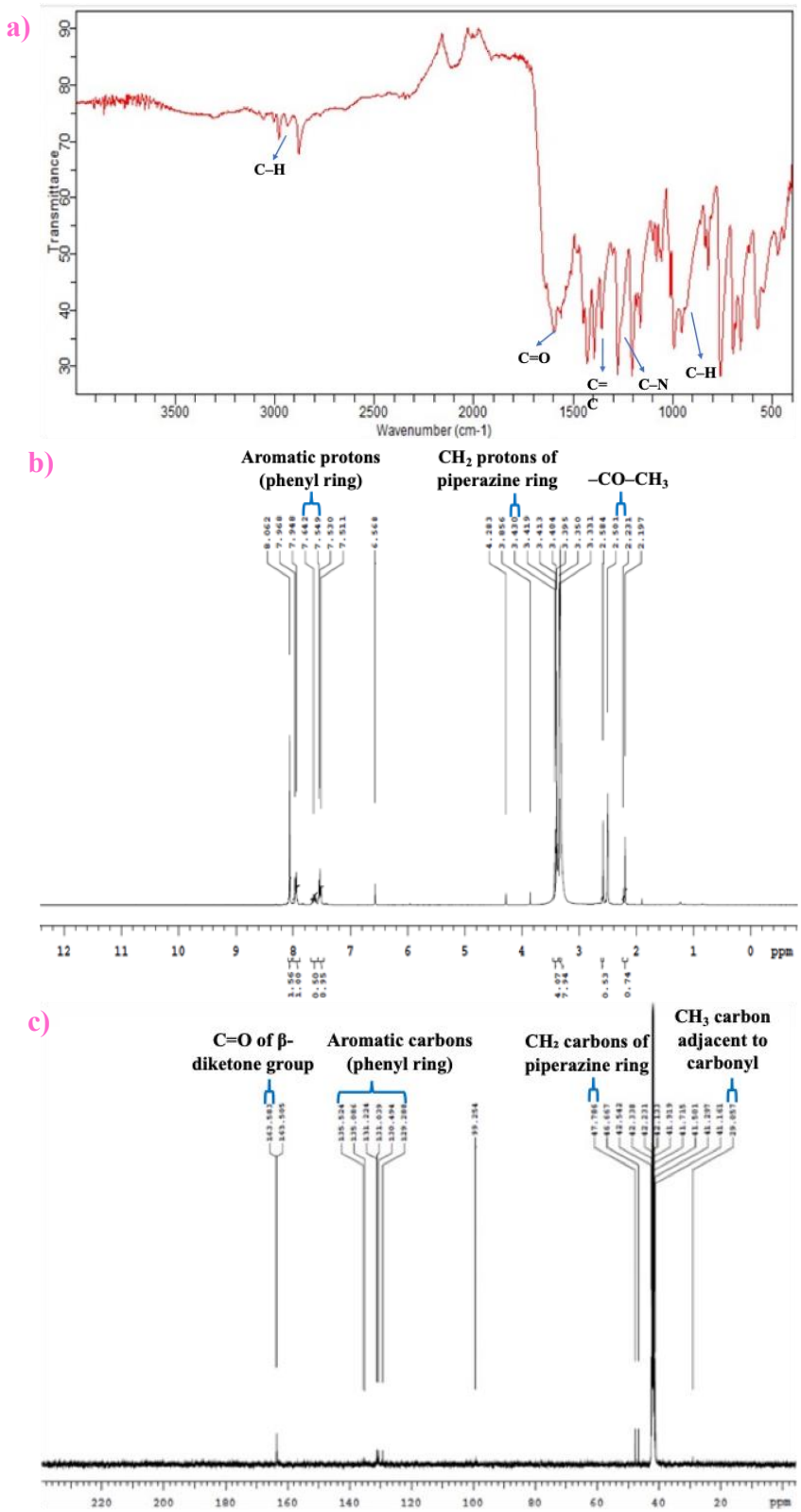

Figure 3. (a) FT-IR spectrum of compound-1d showing characteristic absorption peaks; **(b)** ^{1}H-NMR spectrum highlighting aromatic and aliphatic proton regions; **(c)** ^{13}C-NMR spectrum showing carbonyl, aromatic, and piperazine-carbon signals.

3.2. ADMET analysis.

The ADMET evaluation revealed that compound-1d possesses favorable drug-likeness and pharmacokinetic characteristics compared to Vancomycin. The compound showed excellent intestinal absorption (94.5%) and positive Caco-2 permeability (1.0 log Papp),

indicating strong oral bioavailability. Moderate water solubility (-4.91 log mol/L) supports efficient dissolution during absorption. In terms of distribution, compound-1d exhibited a balanced tissue distribution (VDss = 0.113 log L/kg) and limited blood–brain barrier permeability (-0.233 log BB), which is advantageous for reducing central nervous system side effects. Metabolic profiling predicted CYP3A4 substrate behavior, with selective inhibition of CYP2C19, CYP2C9, and CYP3A4, suggesting manageable metabolism and low potential for drug–drug interactions. The compound showed no mutagenicity in the Ames test and only inhibited hERG II, implying a low genotoxic and cardiotoxic risk. The predicted maximum tolerated dose (-0.085 log mg/kg/day) and non-sensitizing skin response further highlight its favorable safety profile. Overall, the ADMET profile suggests that compound-1d is a promising drug-like molecule, exhibiting strong absorption, moderate distribution, selective metabolism, and a low toxicity risk, which supports its potential as a safer antibacterial lead compared to Vancomycin (Table 1).

Table 1. ADMET property of synthesized compound-1d and Vancomycin.

Property	Model name (Unit)	Predicted value	
		Compound-1d	Vancomycin
Absorption	Water solubility (log mol/L)	-4.914	-2.892
	Caco2 permeability (log Papp in 10^{-6} cm/s)	1	-1.942
	Intestinal absorption (human) (% Absorbed)	94.493	1.59
	Skin Permeability (log Kp)	-2.926	-2.735
	P-glycoprotein substrate	Yes	Yes
	P-glycoprotein I inhibitor	Yes	No
	P-glycoprotein II inhibitor	Yes	Yes
Distribution	VDss (human) (log Log/kg)	0.113	-0.368
	Fraction unbound (human) (Fu)	0	0.37
	BBB permeability (log BB)	-0.233	-5.122
	CNS permeability (log PS)	-2.496	-6.632
Metabolism	CYP2D6 substrate	No	No
	CYP3A4 substrate	Yes	No
	CYP1A2 inhibitor	No	No
	CYP2C19 inhibitor	Yes	No
	CYP2C9 inhibitor	Yes	No
	CYP2D6 inhibitor	No	No
	CYP3A4 inhibitor	Yes	No
Excretion	Total Clearance (log ml/min/kg)	0.647	-1.798
	Renal OCT2 substrate	No	No
Toxicity	AMES toxicity	No	No
	Max. tolerated dose (human) (log mg/kg/day)	-0.085	0.438
	hERG I inhibitor	No	No
	hERG II inhibitor	Yes	No
	Oral Rat Acute Toxicity (LD_{50}) (mol/kg)	2.469	2.482
	Oral Rat Chronic Toxicity (LOAEL) (log mg/kg_bw/day)	1.148	13.271
	Hepatotoxicity	Yes	Yes
	Skin Sensitization	No	No
	T. Pyriformis toxicity (log ug/L)	1.099	0.285
	Minnow toxicity (log mM)	1.844	17.972

3.3. DFT.

3.3.1. Molecular geometry optimization and quantum computation analysis.

DFT calculations were employed to elucidate the theoretical electron density distribution within the compound. Figure 4a illustrates the optimized molecular geometry, including atom numbering, providing crucial insights into the molecular structure. Electronic properties, including the energy levels of the highest occupied molecular orbital (EHOMO)

and the lowest unoccupied molecular orbital (ELUMO), along with the HOMO-LUMO energy gap (Egap) at 6.8329332eV, were computed. EHOMO and ELUMO are associated with the molecule's ionization potential (I) and electron affinity (A), respectively, while the HOMO and LUMO, recognized as frontier orbitals, dictate reactivity and stability. Various reactivity parameters, such as the global electrophilicity index (ω), global hardness (η), chemical potential (-4.19690676eV), and global softness (0.292700066 eV^{-1}), were calculated, providing insights into the compound's stability, reactivity, and potential interactions with biological targets. The higher global hardness implies stability, a substantial energy gap, and lower reactivity.

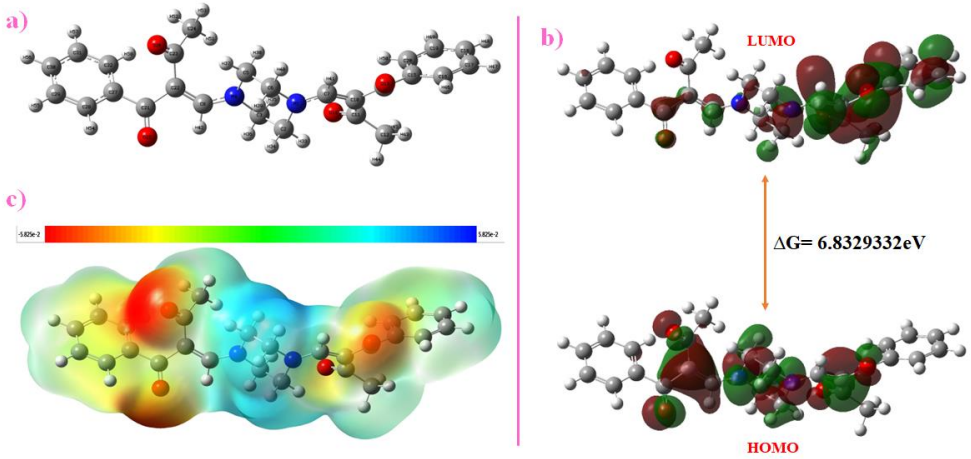

Figure 4. (a) Optimized structure; **(b)** 3-D plot for the electron distribution; **(c)** molecular electrostatic potential of the synthesized compound-1d.

In contrast, the elevated global softness indicates increased reactivity and a greater potential for electron-transfer reactions (Figure 4b). This thorough analysis provides a standardized, comprehensive overview of the compound's electronic and reactivity properties. The detailed information in Table 2 provides a comprehensive overview of the global chemical reactivity profile of the synthesized compound-1d.

The moderate HOMO-LUMO energy gap (6.83 eV) indicates that compound-1d maintains a good balance between molecular stability and chemical reactivity, which is favorable for potential biological activity. The HOMO distribution, primarily localized in the aromatic and carbonyl regions, suggests the presence of possible electron-donating centers. In contrast, the LUMO density, localized over the piperazine and carbonyl oxygen atoms, represents electron-accepting regions. This orbital distribution pattern suggests that these active sites may facilitate charge transfer and hydrogen-bonding interactions with bacterial enzymes, such as PBP2a and glycosyltransferases. Therefore, the electronic configuration of compound-1d supports its observed antibacterial activity by enabling effective interactions with receptor-binding pockets.

Table 2. Global chemical reactivity profile of the synthesized compound-1d.

Parameters	Values
E_{HOMO} (HF)	-0.2797
E_{LUMO} (HF)	-0.0286
E_{HOMO} (eV)	-7.6133
E_{LUMO} (eV)	-0.7804
Energy gap (Δ) (eV)	6.8329
Ionization energy (I) (eV)	7.6133
Electron affinity (A) (eV)	0.7804
Electronegativity (χ) (eV)	4.1969

Parameters	Values
Chemical potential (μ) (eV)	-4.1969
Global hardness (η) (eV)	3.4164
Global softness (s) (eV^{-1})	0.2927
Electrophilicity index (ω) (eV)	2.5778

3.3.2. Molecular electrostatic potential (MEP).

Figure 4c illustrates the MEP map of the synthesized compound-1d, generated using DFT at the CAM-B3LYP++G (2d-p) level of theory. This MEP map reveals distinctive charge density patterns within the molecule, offering crucial insights into its charge distribution. The calculation of MEP involves a comprehensive analysis of the electron density, enabling the anticipation of electrophilic and nucleophilic active regions. The color scale in the MEP diagram indicates varying electrostatic potential, with red to blue. Notably, green-colored regions indicate a neutral electrostatic potential, reflecting a balance of positive and negative charges. Upon examining the MEP map, it becomes evident that oxygen atoms within the molecular structure act as robust electrophilic regions, portrayed by vibrant shades ranging from bright red to orange. These sites are significant as they contribute to the compound's electrophilic reactivity. In contrast, blue-colored regions on the MEP map denote positive electron density, indicating nucleophilic reactivity and suggesting their potential for electron-rich interactions.

These MEP findings support the DFT results by identifying oxygen atoms as strong electrophilic centers likely to form hydrogen bonds with protein residues, and nitrogen atoms in the piperazine ring as nucleophilic regions capable of electrostatic interactions. Such charge distributions are consistent with the active binding orientation observed in docking simulations, highlighting how the compound’s electronic features contribute to its biological activity.

3.4. In-silico studies.

3.4.1. Strategy to combat MRSA.

The Penicillin-binding proteins (PBPs) play a pivotal role in bacterial cell wall biosynthesis by catalyzing transpeptidation of glycan chains, which are crucial for cell wall integrity. Peptidoglycan, comprising glycan chains cross-linked by short-stem peptides, undergoes three sequential stages: cytoplasmic, membrane, and extracellular synthesis. Among these PBPs, bifunctional ones, specifically class A PBPs, perform essential transpeptidation and transglycosylation activities vital for peptidoglycan synthesis. PBP2a, a variant notably resistant to β-lactams such as methicillin, exhibits reduced affinity for cell wall synthesis, thereby hindering bacterial growth. Structurally, PBP2a exhibits an elongated conformation that encompasses a transpeptidase domain and an allosteric site, which contributes to its resistance to conventional β-lactam antibiotics. This altered structure leads to a closed active site, impeding β-lactam access and the formation of acyl-PBP intermediates, consequently reducing susceptibility. Therefore, PBP2a’s modified functionality in catalyzing transpeptidation, while requiring collaboration with other native PBPs for successful peptidoglycan synthesis, underlines its significance in conferring resistance in MRSA strains against β-lactam antibiotics. This additional resistance is attributed to decreased formation of the acyl-PBP intermediate, increased pre-acylation complexation with β-lactams, and the closed nature of the PBP2a active site. PBP2a exhibits reduced susceptibility owing to a closed active site conformation, limiting β-lactam access and formation of acyl-PBP intermediates.

Allosteric binding induces conformational changes that expose the catalytic site for peptidoglycan cross-linking, demonstrating a potential avenue for novel antibiotic development. Targeting the allosteric site could circumvent MRSA resistance, suggesting a promising strategy for combating antibiotic-resistant strains [26–28]. In addition, Bacterial peptidoglycan glycosyltransferases (PGTs) are crucial enzymes that catalyze the polymerization of lipid II into linear glycan chains that form the peptidoglycan structure in bacterial cell walls. The PGT domain, consisting of a large head subdomain and a smaller jaw subdomain, exhibits remarkable specificity and efficiency in lipid II recognition and binding. This recognition is facilitated by motifs within the jaw subdomain, including hydrogen bond interactions involving conserved residues such as Asp101 and Gln136. The jaw subdomain's hydrophobic surface and dynamic 'flap' region play pivotal roles in anchoring onto the cell membrane and capturing the lipid II substrate.

Furthermore, the interaction between PGT and lipid II occurs within a crowded environment of membrane phospholipids, suggesting a mechanism in which the jaw subdomain, resembling amphipathic cationic α-helical antimicrobial peptides (ACAH AMPs), selectively targets and captures lipid II from the membrane. The binding of lipid II in the PGT active site induces allosteric motions, thereby enhancing the positive cooperativity between the donor and acceptor sites, which is crucial for the processive elongation of the glycan chain. This process involves reorganizing the GT active site through structural rearrangements induced by the binding of lipid II or lipid IV, thereby facilitating peptidoglycan biosynthesis (Figure 5) [29–31].

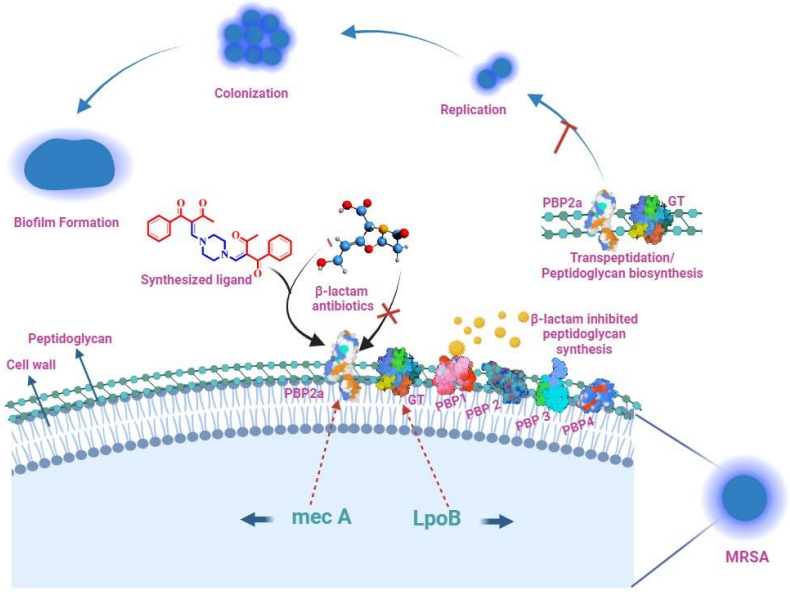

Figure 5. Pictorial representation of the mechanism involved in PBP2a and PBP1b of MRSA.

3.4.2. Molecular docking.

The docking analysis results demonstrate significant interactions between the designed compounds and the protein PBP2a. Compound-1a exhibits a binding energy of -6.6 kcal/mol, Compound-1b has -6.5 kcal/mol, Compound-1c -7.0 kcal/mol, whereas Compound-1d demonstrates the highest binding energy of -8.8 kcal/mol. Compound-1d exhibits a remarkable affinity, forming hydrogen bonds, π-anion, π-alkyl, and carbon–hydrogen interactions with various amino acid residues. Specifically, conventional hydrogen bonds are formed with amino residues SER598, SER403, SER462, TYR446, and ASN464 in 1MWT, along with the observation of a Pi–Anion bond with GLU602. To understand the importance of these

interactions, the standard MRSA drug, Vancomycin, was docked at the same active site as the synthesized compound 1d. This comparative examination indicates a similar interaction pattern with amino acid residues SER403 and TYR446 for both Vancomycin and compound-1d in protein 1MWT (Figure 6).

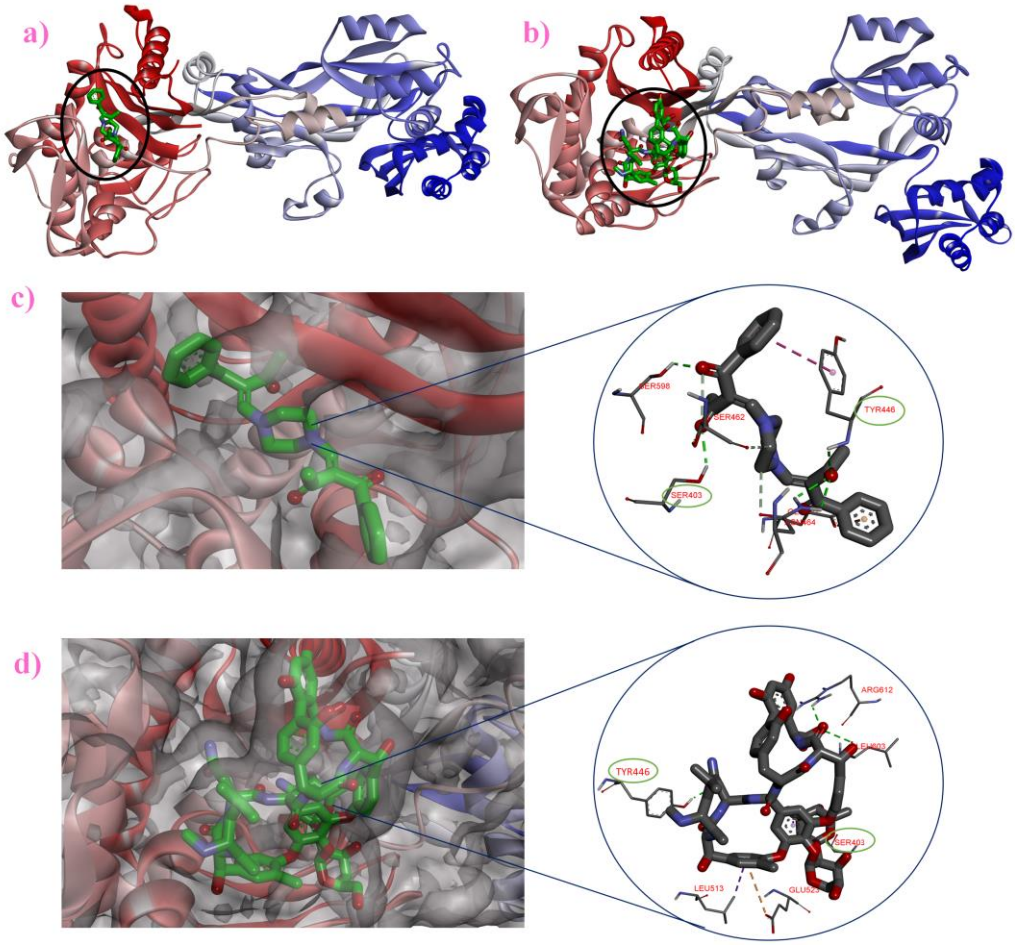

Figure 6. 3D-interaction of PBP2a protein with **(a,c)** compound-1d; **(b,d)** Vancomycin.

Docking results with glycosyltransferase (6FTB) show that Compound-1a exhibits a binding energy of -6.4 kcal/mol, Compound-1b -6.5 kcal/mol, and Compound-1c -6.7 kcal/mol, whereas Compound-1d demonstrates the highest binding energy of -7.1 kcal/mol. Protein 6FTB demonstrates enhanced interactions with compound-1d, forming hydrogen bonds with residues GLY131, SER132, LYS140, TYR181, and ASN141, along with carbon–hydrogen bonds involving GLN137, VAL223, and ASN224, and a Pi–Alkyl bond with PRO226. Vancomycin docking at the same active site revealed shared residues SER132, LYS140, and ASN224, confirming binding site overlap and mechanism similarity (Figure 7 and Table 3).

To validate docking accuracy, re-docking of compound-1d was performed, and the root mean square deviation (RMSD) of the best docking poses remained below 2.0 Å, confirming pose reproducibility and structural stability within the active site. Additionally, consensus scoring was applied across multiple docking runs to eliminate outliers and ensure the reliability of the predicted binding affinities. These validation steps confirm that the docking predictions for compound-1d are statistically consistent and reproducible, providing confidence in the comparative analysis with Vancomycin.

When compared with the mechanism underlying bacterial resistance, particularly the role of PBP2a and GT, the docking interactions resonate profoundly. The docking results

display notable interactions with amino acid residues crucial for the stability of proteins involved in cell wall synthesis, which aligns with the proposed mechanism of action.

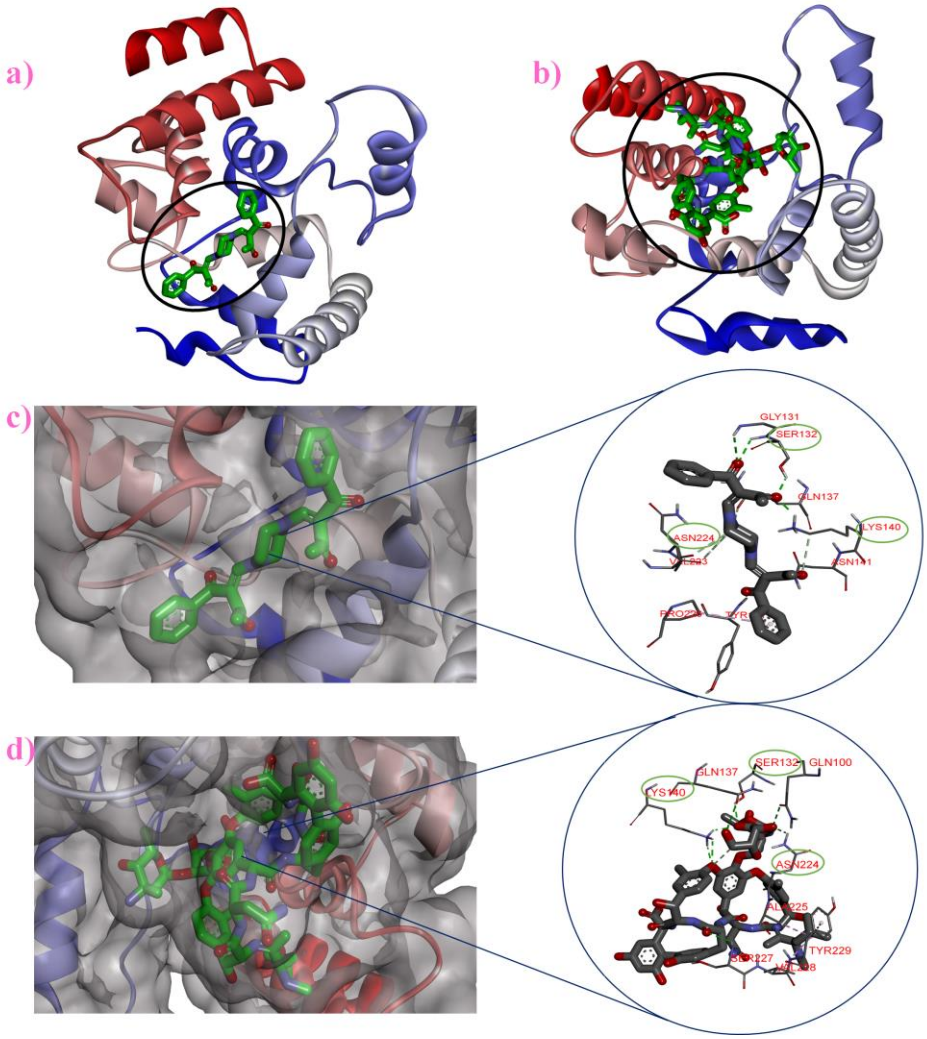

Figure 7. 3D-interaction of Glycosyltransferase protein with **(a,c)** compound-1d; **(b,d)** Vancomycin.

These interactions appear to target key residues associated with protein stability, such as SER403, TYR446, and ASN224, which are linked to cell wall strengthening and antibacterial resistance, thereby confirming a potential impact on bacterial cell growth and division. Integrating these docking outcomes with the mechanism underscores the likelihood that our ligand can influence protein stability and functionality in cell wall synthesis pathways, potentially disrupting bacterial growth and offering a promising avenue for further investigation and the development of antibacterial agents. This alignment between docking interactions and the mechanism provides valuable insights into the ligand's potential impact on bacterial resistance pathways, underscoring its therapeutic potential.

Table 3. Molecular docking analysis for compound-1d with MRSA proteins.

PDB ID	Ligand	Key interacting residues	Major interaction types	Binding energy (kcal/mol)
1MWT	Compound-1d	SER403, TYR446, ASN464, SER598	H-bond, π–π interaction	-8.8
	Vancomycin	SER403, TYR446, ARG612	H-bond, π–anion interaction	-6.9
6FTB	Compound-1d	SER132, LYS140, ASN141, ASN224, PRO226	H-bond, C–H, π–alkyl interaction	-7.1
	Vancomycin	SER132, LYS140, ASN224, TYR229	H-bond, π–alkyl interaction	-8.3

3.4.3. Molecular dynamics simulation.

Molecular dynamics (MD) simulations were performed for both the 1MWT (PBP2a) and 6FTB (Glycosyltransferase) protein–ligand complexes for 100 ns to assess their dynamic stability and conformational behavior. Key parameters, including root mean square deviation (RMSD), root mean square fluctuation (RMSF), solvent accessible surface area (SASA), radius of gyration (Rg), hydrogen bonding, and Gibbs free energy landscape, were analyzed to understand structural stability and binding persistence of compound-1d within the active sites.

The RMSD profiles (Figures 8a and 8b) show that both complexes achieved equilibrium within the first 20 ns and remained stable throughout the 100-ns trajectory. The ligand in the 1MWT complex displayed two equilibrium conformations before and after 68 ns, with overall deviations between 2.0 and 3.5 Å. In contrast, the 6FTB complex exhibited moderate fluctuations (2.6-4.1 Å), indicating flexible yet stable binding. The RMSF plots (Figure 8c and 8d) revealed higher fluctuations at loop regions in 1MWT, while core residues remained stable. The lower RMSF amplitude in 6FTB (average 1.8 Å) compared to 1MWT (average 2.3 Å) suggests that the glycosyltransferase complex is comparatively more rigid and stable.

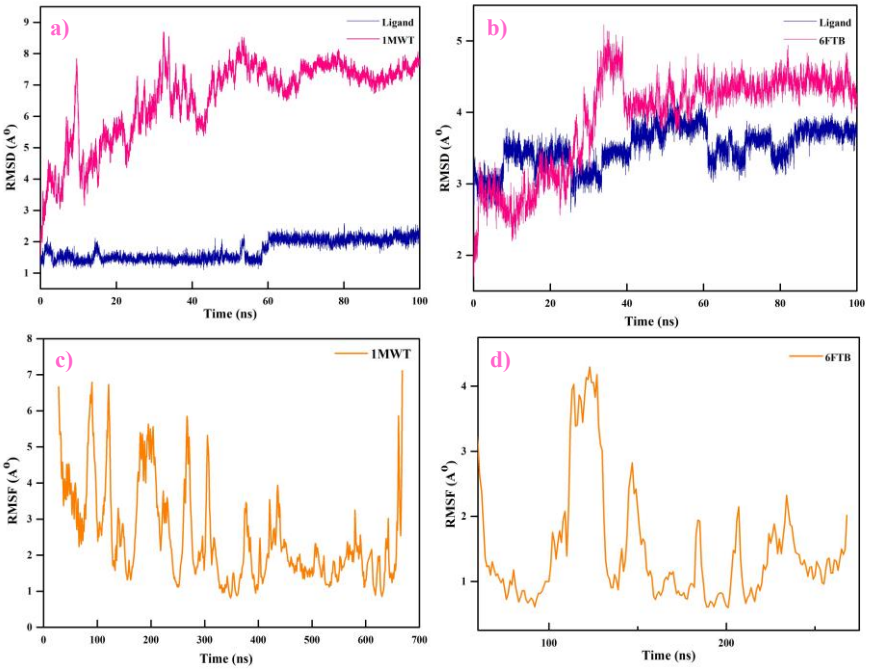

Figure 8. (a, b) RMSD; **(c, d)** RMSF plots for compound-1d with MRSA proteins.

The SASA and Rg analyses (Figure 9) indicate gradual compaction of both proteins during the simulation. The solvent-accessible surface area of 1MWT decreased from 3425 Å² to 2961 Å², and that of 6FTB from 1232 Å² to 1062 Å², indicating reduced solvent exposure and improved folding stability. Similarly, the radius of gyration decreased from 37.2 Å to 35.9 Å for 1MWT and from 17.9 Å to 17.3 Å for 6FTB, confirming enhanced compactness.

The hydrogen bond analysis (Figure 10a and 10b) showed persistent intramolecular bonding across the simulation, maintaining an average of 507 hydrogen bonds in 1MWT and 180 in 6FTB. These stable hydrogen networks contribute to the structural integrity of both complexes. The Gibbs free energy landscapes (Figure 10c and10d) further illustrate that 6FTB exhibits deeper low-energy basins (dark blue regions), suggesting greater thermodynamic stability than 1MWT, which displayed broader energy distributions.

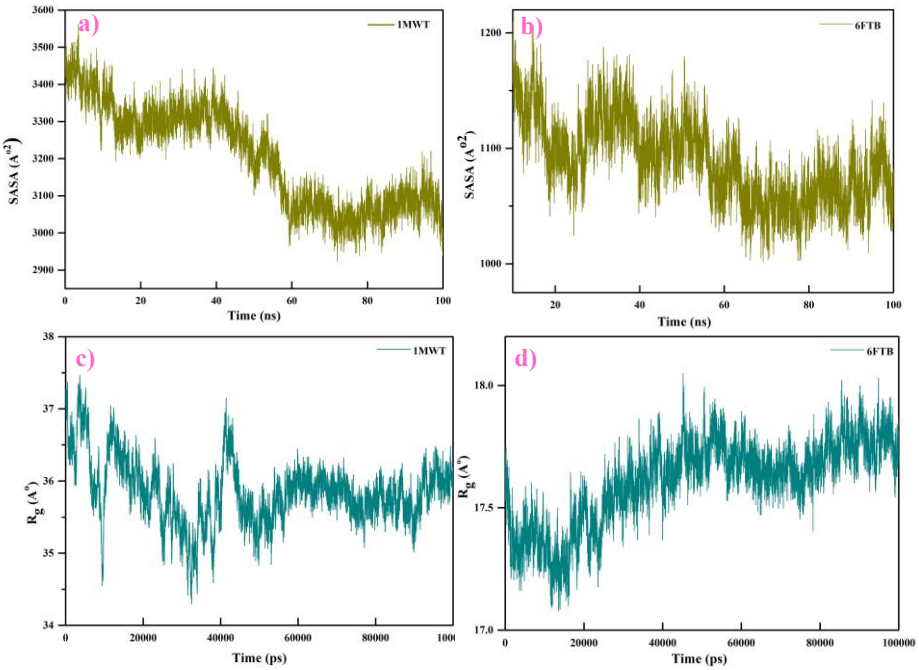

Figure 9. (a, b) SASA; **(c, d)** Rg plots for compound-1d with MRSA proteins.

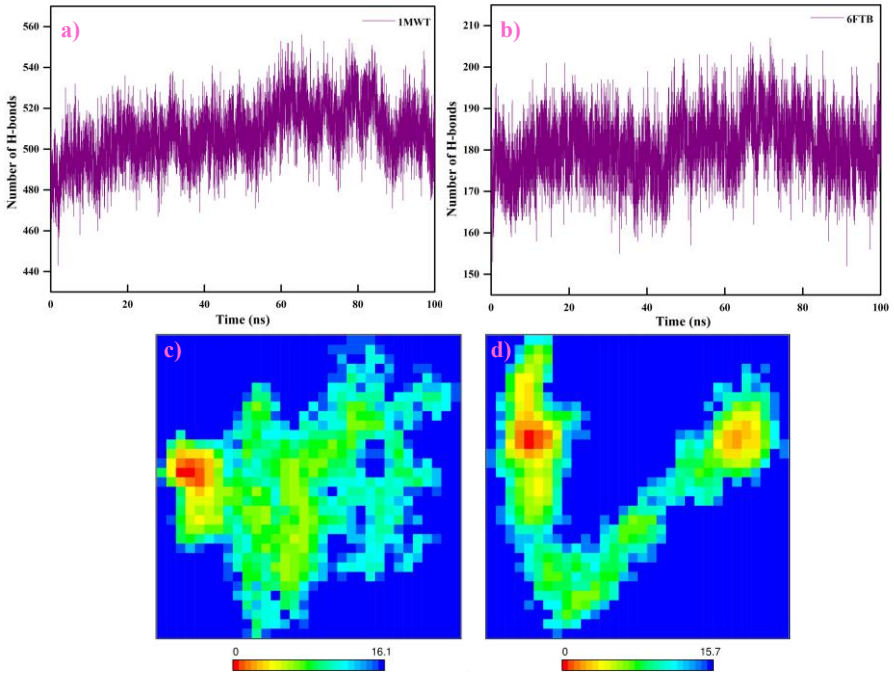

Figure 10. Hydrogen bonding and Gibbs free energy landscapes for compound-1d with MRSA proteins.

Overall, MD results confirm that compound-1d forms strong, stable, and long-lasting interactions with both target proteins, with the 6FTB complex showing slightly higher compactness and thermodynamic stability. This dynamic behavior complements the docking and DFT results, validating the molecular robustness and antibacterial potential of compound-1d as an effective MRSA inhibitor.

3.5. Antibacterial studies.

The antibacterial activity of the synthesized compound 1d was evaluated using the broth dilution method against MRSA. The MIC and MBC were determined to assess bacteriostatic and bactericidal effects, respectively. The MIC was 125 µg/mL, indicating the lowest concentration that inhibited visible bacterial growth. In comparison, the MBC was 250 µg/mL,

representing the concentration required to eliminate bacterial viability (Figure 11). All experiments were performed in triplicate, and the mean absorbance values (OD_{570} ± SD) were calculated to ensure reproducibility. The variation among replicates remained below 5%, confirming the assay's consistency and accuracy. Quantitative MIC/MBC results are summarized in Table 4, showing a dose-dependent decline in bacterial growth with increasing ligand concentration. The complete absence of purple coloration at 250 µg/mL confirmed bactericidal activity, whereas reduced coloration at 125 µg/mL corresponded to growth inhibition.

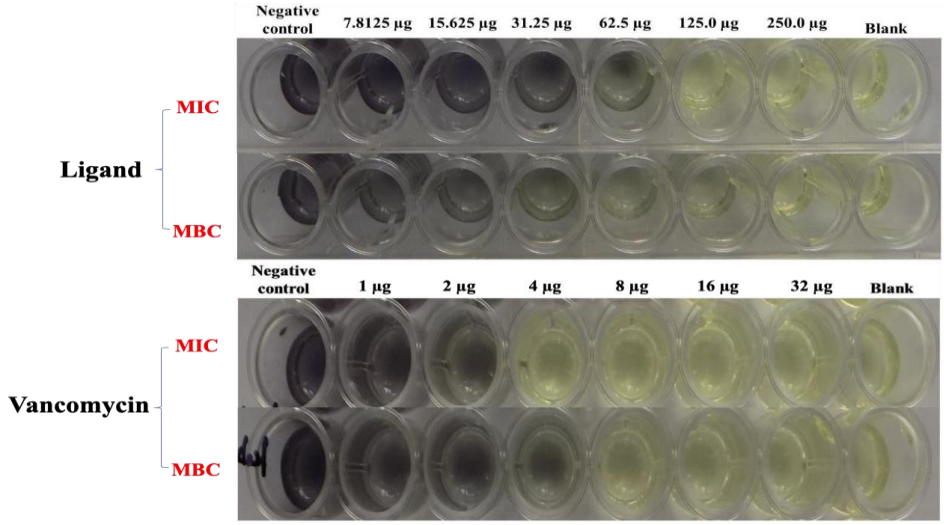

Figure 11. Pictorial representation of antibacterial activity trials of (**a)** Ligand; (**b)** Standard (Vancomycin).

Table 4. MIC and MBC assay results showing mean OD_{570} values (± SD) at different concentrations of compound-1d (n = 3).

Concentration (µg/mL)	Mean OD_{570} ± SD	% Growth (vs control)
Negative Control (0)	0.1 ± 0.01	100%
7.8125	0.942 ± 0.03	94.20%
15.625	0.850 ± 0.04	85.00%
31.25	0.621 ± 0.05	62.10%
62.5	0.398 ± 0.03	39.80%
125	0.082 ± 0.02	8.20%
250	0.000 ± 0.00	0%

These results demonstrate moderate but consistent antibacterial efficacy of compound-1d compared to Vancomycin, which served as the standard control. The observed inhibitory action can be directly correlated with the compound's strong binding affinity toward PBP2a and GT, as revealed by docking and molecular dynamics studies. Compound-1d exhibited significant hydrogen bonding and π–anion interactions at active site residues (SER403, TYR446, ASN224, and PRO226), which are critical for the enzymes' catalytic function.

Integrating in-silico and in-vitro findings, the docking and MD simulations confirm that compound-1d maintains stable conformations within both enzyme-binding pockets, thereby reducing the flexibility and accessibility of the active sites essential for peptidoglycan cross-linking. This structural interference effectively impairs transpeptidation and glycan polymerization, leading to cell wall weakening and bacterial lysis, as supported by MIC/MBC data. Moreover, the compound's favorable ADMET profile and high thermodynamic stability further support its ability to maintain biological efficacy under physiological conditions.

Overall, the combined computational and experimental evidence substantiates a dual-action antibacterial mechanism, in which compound-1d exerts enzyme inhibition (targeting

PBP2a and GT) and disrupts membrane-associated cell wall synthesis. This mechanistic complementarity highlights its potential as a promising lead molecule against MRSA.

4. Conclusions

This study presents a rationally designed piperazine-coupled 1,3-diketone derivative (compound-1d) as a potential anti-MRSA agent. The hybrid framework integrates two pharmacophoric motifs, piperazine for solubility and flexibility, and β-diketone for enhanced hydrogen-bonding potential, resulting in a structurally stable and biologically active scaffold. Structural characterization (FT-IR, ^{1}H-NMR, ^{13}C-NMR) confirmed successful synthesis and purity, while ADMET and DFT analyses demonstrated favorable drug-likeness, high stability (Egap = 6.83 eV), and low predicted toxicity, establishing its viability as a lead molecule.

In silico investigations revealed strong, consistent binding interactions with key MRSA proteins. Docking studies revealed notable binding energies of -8.8 kcal/mol (PBP2a) and -7.1 kcal/mol (Glycosyltransferase), supported by RMSD values of ≤ 2.0 Å and consensus scoring validation. Molecular dynamics simulations further confirmed the formation of stable protein–ligand complexes, characterized by compact structural conformations and persistent hydrogen bonding throughout the 100-ns trajectory. These computational insights correlate well with the observed antibacterial activity, with the compound exhibiting an MIC of 125 µg/mL and an MBC of 250 µg/mL against MRSA (ATCC-43300). The results suggest that the compound likely disrupts PBP2a- and GT-mediated cell-wall synthesis, impairing bacterial growth and survival.

While the findings highlight compound-1d as a promising and mechanistically validated anti-MRSA scaffold, further optimization and biological validation are warranted. Future work will focus on evaluating cytotoxicity in mammalian cell lines, followed by *in vivo* efficacy studies to assess pharmacokinetics, therapeutic index, and safety profile. Such efforts will advance this compound from preliminary validation toward the development of a next-generation antibacterial candidate capable of combating resistant MRSA strains.

Author Contributions

Conceptualization, C.S.K.; methodology, N.G.N.; software, N.G.N.; data curation, C.S.K.; writing—original draft preparation, N.G.N.; writing—review and editing, N.G.N., S.N., S.A.S., and C.S.K.; supervision, C.S.K. All authors have read and agreed to the published version of the manuscript.

Institutional Review Board Statement

Not applicable.

Informed Consent Statement

Not applicable.

Data Availability Statement

All data generated or analyzed during this study are included in this published article.

Funding

This research received no external funding.

Acknowledgments

The authors are thankful to JSSSTU for providing computing facilities.

Conflicts of Interest

The authors declare that they have no conflict of interest.

References

1. Hamad, M.; Al-Marzooq, F.; Srinivasulu, V.; Omar, H.A.; Sulaiman, A.; Zaher, D.M.; Orive, G.; Al-Tel, T.H. Antibacterial Activity of Small Molecules Which Eradicate Methicillin-Resistant Staphylococcus Aureus Persisters. *Front. Microbiol.* **2022**, *13*, 823394, doi:10.3389/fmicb.2022.823394.
2. Yang, J.; Brown, C.; Noland, W.; Johnson, T.J.; Ji, Y. Identification and Validation of a Novel Antibacterial Compound MZ-01 against Methicillin-Resistant Staphylococcus Aureus. *Antibiotics* **2022**, *11*, 1550, doi:10.3390/antibiotics11111550.
3. Guan, S.; Yu, H.; Xiang, H.; Wang, L.; Liu, J.; Wu, A.; Zheng, J.; Dong, H.; Wang, L.; Wang, D. WYBQ-4: A New Bactericidal Agent against Methicillin-Resistant Staphylococcus Aureus. *Microbiol. Spectr.* **2022**, *10*, e00547-22, doi:10.1128/spectrum.00547-22.
4. Dey, R.; De, K.; Mukherjee, R.; Ghosh, S.; Haldar, J. Small Antibacterial Molecules Highly Active against Drug-Resistant *Staphylococcus Aureus*. *MedChemComm* **2019**, *10*, 1907–1915, doi:10.1039/C9MD00329K.
5. Aggarwal, S.; Jain, D.; Kaur, P.; Singh, K. Advances in Piperazine-Based Compounds for Antimicrobial DrugDevelopment: Design, SAR, and Therapeutic Potential. *Curr. Drug Res. Rev.* **2025**, *17*, doi:10.2174/0125899775378431250611100229.
6. Prasad, H.S.N.; Ananda, A.P.; Mukarambi, A.; Gaonkar, N.P.; Sumathi, S.; Spoorthy, H.P.; Mallu, P. Design, Synthesis, and Anti-Bacterial Activities of Piperazine Based Phthalimide Derivatives against Superbug-Methicillin-Resistant Staphylococcus Aureus. *Curr. Chem. Lett.* **2023**, *12*, 65–78, doi:10.5267/j.ccl.2022.9.005.
7. Antibacterial Property of Schiff-Based Piperazine against MRSA: Design, Synthesis, Molecular Docking, and DFT Computational Studies. *Lett. Appl. NanoBioScience* **2022**, *12*, 54, doi:10.33263/LIANBS122.054.
8. Patel, R.V.; Park, S.W. Synthesis of Highly Potent Piperazine-Linked Benzothiazolyl-4-Thiazolidinones via Catalytic N-Formylation: Antibacterial Drug Design. *Med. Chem. Res.* **2014**, *23*, 4099–4107, doi:10.1007/s00044-014-0987-z.
9. Thomas, G.L.; Spandl, R.J.; Glansdorp, F.G.; Welch, M.; Bender, A.; Cockfield, J.; Lindsay, J.A.; Bryant, C.; Brown, D.F.J.; Loiseleur, O.; et al. Anti-MRSA Agent Discovery Using Diversity-Oriented Synthesis. *Angew. Chem. Int. Ed.* **2008**, *47*, 2808–2812, doi:10.1002/anie.200705415.
10. Romanelli, M.N.; Manetti, D.; Braconi, L.; Dei, S.; Gabellini, A.; Teodori, E. The Piperazine Scaffold for Novel Drug Discovery Efforts: The Evidence to Date. *Expert Opin. Drug Discov.* **2022**, *17*, 969–984, doi:10.1080/17460441.2022.2103535.
11. Bouley, R.; Kumarasiri, M.; Peng, Z.; Otero, L.H.; Song, W.; Suckow, M.A.; Schroeder, V.A.; Wolter, W.R.; Lastochkin, E.; Antunes, N.T.; et al. Discovery of Antibiotic (*E*)-3-(3-Carboxyphenyl)-2-(4-Cyanostyryl)Quinazolin-4(3 *H*)-One. *J. Am. Chem. Soc.* **2015**, *137*, 1738–1741, doi:10.1021/jacs.5b00056.
12. Shabestarian, A.; Pordel, M.; Bozorgmehr, M.R. Design and Evaluation of an Imidazoacridine-Penicillin Hybrid: A Dual-Action Strategy Against Multidrug-Resistant Bacteria. *ChemistrySelect* **2025**, *10*, e01417, doi:10.1002/slct.202501417.
13. La Monica, G.; Gallo, A.; Bono, A.; Alamia, F.; Lauria, A.; Alduina, R.; Martorana, A. Novel Antibacterial 4-Piperazinylquinoline Hybrid Derivatives Against Staphylococcus Aureus: Design, Synthesis, and In Vitro and In Silico Insights. *Molecules* **2024**, *30*, 28, doi:10.3390/molecules30010028.
14. Saini, S.; Reddy, G.L.; Gangwar, A.; Kour, H.; Nadre, G.G.; Pandian, R.; Pal, S.; Nandi, U.; Sharma, R.; Sawant, S.D. Discovery and Biological Evaluation of Nitrofuranyl–Pyrazolopyrimidine Hybrid Conjugates as Potent Antimicrobial Agents Targeting *Staphylococcus Aureus* and Methicillin-Resistant *S. Aureus*. *RSC Med. Chem.* **2025**, *16*, 1304–1328, doi:10.1039/D4MD00826J.
15. Punith, M.S.; Ningaraju, G.N.; Nanjundaswamy, S.; Chethana, M.H.; Sandeep, S.; Santhosh, A.S.; Rajabathar, J.R.; Karthik, C.S.; Mallu, P. 2,4-Difluorophenyl(Piperidin-4-Yl) Methanoneoxime Derivatives as Potent Contenders to Combat Antibacterial Resistance of MRSA: In-Silico Approach. *Discov. Mol.* **2025**, *2*, doi:10.1007/s44345-025-00010-2.

16. Prakash, P.; Misra, A.; Surin, W.R.; Jain, M.; Bhatta, R.S.; Pal, R.; Raj, K.; Barthwal, M.K.; Dikshit, M. Anti-Platelet Effects of Curcuma Oil in Experimental Models of Myocardial Ischemia-Reperfusion and Thrombosis. *Thromb. Res.* **2011**, *127*, 111–118, doi:10.1016/j.thromres.2010.11.007.
17. El Bakri, Y.; Anouar, E.H.; Ramli, Y.; Essassi, E.M.; Mague, J.T. Synthesis, Crystal Structure, Spectroscopic Characterization, Hirshfeld Surface Analysis, and DFT Calculations of 1,4-Dimethyl-2-Oxo-Pyrimido[1,2-a]Benzimidazole Hydrate. *J. Mol. Struct.* **2018**, *1152*, 154–162, doi:10.1016/j.molstruc.2017.09.074.
18. Usman, M.; Khan, R.A.; Alsalme, A.; Alharbi, W.; Alharbi, K.H.; Jaafar, M.H.; Abu Khanjer, M.; Tabassum, S. Structural, Spectroscopic, and Chemical Bonding Analysis of Zn(II) Complex [Zn(Sal)](H2O): Combined Experimental and Theoretical (NBO, QTAIM, and ELF) Investigation. *Crystals* **2020**, *10*, 259, doi:10.3390/cryst10040259.
19. Jayashankar, J.; Ningaraju, G.N.; Nanjundaswamy, S.; Rajabathar, J.R.; Karnan, M.; Karthik, C.S.; Mallu, P. An In-Silico Investigation of Volatile Compounds in Tulsi and Ginger as a Potent Inhalant for SARS-CoV-2 Treatment. *J. Iran. Chem. Soc.* **2024**, *21*, 479–502, doi:10.1007/s13738-023-02939-y.
20. Rani, N.; Vijayakumar, S.; P.T.V., L.; Arunachalam, A. Allosteric Site-Mediated Active Site Inhibition of PBP2a Using Quercetin 3-O-Rutinoside and Its Combination. *J. Biomol. Struct. Dyn.* **2016**, *34*, 1778–1796, doi:10.1080/07391102.2015.1092096.
21. Prashanth, D.P.; Ningaraju, G.N.; Rangappa, S.; Rangappa, K.S.; Karthik, C.S. Exploring the Potential of Thiazole Derivatives in Modulating the Wnt/β-Catenin Pathway for Colon Cancer Therapy. *Discov. Mol.* **2025**, *2*, doi:10.1007/s44345-025-00015-x.
22. Van Der Spoel, D.; Lindahl, E.; Hess, B.; Groenhof, G.; Mark, A.E.; Berendsen, H.J.C. GROMACS: Fast, Flexible, and Free. *J. Comput. Chem.* **2005**, *26*, 1701–1718, doi:10.1002/jcc.20291.
23. Schüttelkopf, A.W.; Van Aalten, D.M.F. *PRODRG* : A Tool for High-Throughput Crystallography of Protein–Ligand Complexes. *Acta Crystallogr. D Biol. Crystallogr.* **2004**, *60*, 1355–1363, doi:10.1107/S0907444904011679.
24. Agyare, C.; Koffuor, G.A.; Boamah, V.E.; Adu, F.; Mensah, K.B.; Adu-Amoah, L. Antimicrobial and Anti-Inflammatory Activities of *Pterygota Macrocarpa* and *Cola Gigantea* (Sterculiaceae). *Evid. Based Complement. Alternat. Med.* **2012**, *2012*, 1–9, doi:10.1155/2012/902394.
25. Cos, P.; Vlietinck, A.J.; Berghe, D.V.; Maes, L. Anti-Infective Potential of Natural Products: How to Develop a Stronger in Vitro 'Proof-of-Concept.' *J. Ethnopharmacol.* **2006**, *106*, 290–302, doi:10.1016/j.jep.2006.04.003.
26. Lim, D.; Strynadka, N.C.J. Structural Basis for the β Lactam Resistance of PBP2a from Methicillin-Resistant Staphylococcus Aureus. *Nat. Struct. Biol.* **2002**, doi:10.1038/nsb858.
27. Guignard, B.; Entenza, J.; Moreillon, P. β-Lactams against Methicillin-Resistant. *Curr. Opin. Pharmacol.* **2005**, *5*, 479–489, doi:10.1016/j.coph.2005.06.002.
28. Shalaby, M.-A.W.; Dokla, E.M.E.; Serya, Rabah.A.T.; Abouzid, K.A.M. Penicillin Binding Protein 2a: An Overview and a Medicinal Chemistry Perspective. *Eur. J. Med. Chem.* **2020**, *199*, 112312, doi:10.1016/j.ejmech.2020.112312.
29. Hao, H.; Cheng, G.; Dai, M.; Wu, Q.; Yuan, Z. Inhibitors Targeting on Cell Wall Biosynthesis Pathway of MRSA. *Mol. Biosyst.* **2012**, *8*, 2828, doi:10.1039/c2mb25188d.
30. Derouaux, A.; Sauvage, E.; Terrak, M. Peptidoglycan Glycosyltransferase Substrate Mimics as Templates for the Design of New Antibacterial Drugs. *Front. Immunol.* **2013**, *4*, doi:10.3389/fimmu.2013.00078.
31. Punekar, A.S.; Samsudin, F.; Lloyd, A.J.; Dowson, C.G.; Scott, D.J.; Khalid, S.; Roper, D.I. The Role of the Jaw Subdomain of Peptidoglycan Glycosyltransferases for Lipid II Polymerization. *Cell Surf.* **2018**, *2*, 54–66, doi:10.1016/j.tcsw.2018.06.002.

Publisher's Note & Disclaimer

The statements, opinions, and data presented in this publication are solely those of the individual author(s) and contributor(s) and do not necessarily reflect the views of the publisher and/or the editor(s). The publisher and/or the editor(s) disclaim any responsibility for the accuracy, completeness, or reliability of the content. Neither the publisher nor the editor(s) assume any legal liability for any errors, omissions, or consequences arising from the use of the information presented in this publication. Furthermore, the publisher and/or the editor(s) disclaim any liability for any injury, damage, or loss to persons or property that may result from the use of any ideas, methods, instructions, or products mentioned in the content. Readers are encouraged to independently verify any information before relying on it, and the publisher assumes no responsibility for any consequences arising from the use of materials contained in this publication.